Modeling and Measurements on a Finite Rectangular Conducting Plate in an Eddy Current Damper

K. J. W. Pluk, *Student Member, IEEE*, T. A. van Beek, J. W. Jansen, *Member, IEEE*, and E. A. Lomonova, *Senior Member, IEEE*

***Abstract*—This paper concerns the modeling of an eddy current damper with a finite conducting plate. In the eddy current damper, a finite rectangular conducting plate is moving between cuboidal magnets. The first step of the modeling method is based on an infinite conducting plate. For this infinite conducting plate, the eddy current density is derived using two different methods, the scalar potential method and the vector potential method. The finite boundaries of the conducting plate are included by means of the method of images in two dimensions and, therewith, complete the model. By applying the method of images, the accuracy of the models for calculating the damping coefficient is significantly improved. The assumption of an infinite conducting plate gives less than 15% error for a conducting plate with at least twice the dimensions of the permanent magnet. Applying the method of images reduces the modeling error for a conducting plate with two times the permanent-magnet dimensions to less than 3% in respect to a finite-element model. For the verification of the semi-analytical model, measurements are performed. For a variation of the plate width, the presented semianalytical model has less than 5% discrepancy with respect to the measurements.**

***Index Terms*—Eddy current damping, eddy currents, electromagnetic forces, electromagnetic modeling, finite-element method (FEM), magnetic devices, method of images, permanent magnets.**

NOMENCLATURE

$\vec{A}$	Magnetic vector potential.
$\vec{B}$	Magnetic flux density.
$\vec{E}$	Electric field strength.
$\vec{F}_d$	Damping force.
$\vec{J}_e$	Eddy current density.
$\vec{e}$	Unit vector.
B_r	Remanent flux density of permanent magnet.
J	Current density.
M_s	Magnetization of a permanent magnet.
d	Damping coefficient.
v	Velocity of the conducting plate.
x_n, y_m, z_k	Corner coordinates of permanent magnet.
μ_0	Permeability of vacuum $4\pi \cdot 10^{-7}$ H/m.
σ	Conductivity.
σ_m	Magnetic equivalent charge.
$\widetilde{A}$	Three-dimensional Fourier transform of $\vec{A}$.
$\widetilde{J}$	Three-dimensional Fourier transform of $\vec{J}_e$.
$\mathcal{F}_q^{-1}, \mathcal{F}_q$	(Inverse) Fourier transform to q.
$\boldsymbol{E}, \boldsymbol{X}, \boldsymbol{Y}$	Matrix representation.
AM	(Semi-)Analytical model.
AM-M	(Semi-)Analytical model with mirrors.
FEM	Finite-element method.
SPM	Scalar potential method.
VPM	Vector potential method.

Manuscript received March 8, 2013; revised July 17, 2013; accepted August 4, 2013. Date of publication August 22, 2013; date of current version February 7, 2014. This work was supported by MECAL Applied Mechanics.

The authors are with the Electromechanics and Power Electronics Group, Department of Electrical Engineering, Eindhoven University of Technology, 5612 AZ Eindhoven, The Netherlands (e-mail: K.J.W.Pluk@tue.nl; T.A.v.beek@student.tue.nl; j.w.jansen@tue.nl; e.lomonova@tue.nl).

Color versions of one or more of the figures in this paper are available online at http://ieeexplore.ieee.org.

Digital Object Identifier 10.1109/TIE.2013.2279364

I. INTRODUCTION

MODERN electromagnetic applications have ever increasing requirements. Unfortunately, there are many parasitic effects in these applications, and they are becoming the limiting factor for their performance. One of these performance-decreasing effects is the occurrence of eddy currents [1], [2]. Every conductive material which experiences a change in magnetic field will induce eddy currents, desired [3] or undesired [4]. To accurately predict eddy current phenomena, this paper derives the eddy currents occurring in an eddy current damper [5]. In an eddy current damper, the conductive material is experiencing a traveling magnetic field, or the conductive material is moving in a stationary magnetic field. These eddy currents create a force counteracting the movement. The modeling of electromagnetic devices is commonly done by means of numerical methods (finite-element analysis [6]–[8]) or by (semi-)analytical models [9]–[13].

Most analytical and semianalytical modeling techniques for eddy current phenomena assume that the eddy currents are induced in a predefined coil or in a conducting material which has an infinitely small thickness and infinite dimensions in the direction of the eddy currents [14]. However, when the size of the conducting material is comparable to the dimensions of the source of the magnetic field, the modeling error made by assuming an infinite conductor is significant. The configuration of a passive eddy current damper with two permanent magnets and a conductive plate is illustrated in Fig. 1(b). In case of a cylindrical conductor, the method of images is frequently used to mimic the finite dimensions of this conductor [15], [16]. Applying the method of images in two dimensions on the electrostatic field solutions in rectangular wave guides [17], [18] is a known practice.

This paper applies the method of images to extract the eddy current density in a finite rectangular plate. A 3-D semianalytical modeling method is proposed to calculate the damping force in a passive eddy current device. Instead of neglecting the error

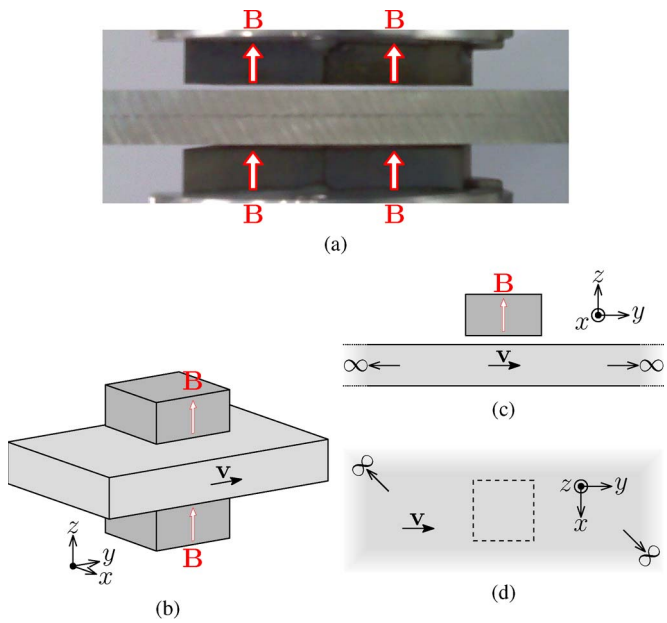

Fig. 1. (a) Real eddy current damper with permanent magnets, (b) the full 3-D topology concerned in the modeling, and the (c) side view and (d) top view of the topology of the eddy current damper simplified to one magnet.

made with assuming that the conducting plate is infinite (as it is done in [19]) or approximating a rectangular conducting plate by a cylindrical one (see [5]), this paper uses the method of images in two dimensions to include the finite boundaries of the rectangular conducting plate. For verification, a 3-D finite-element analysis model is used. The semianalytical modeling method, both with and without finite boundaries, is compared for a variation in the dimensions of the conductive plate with respect to the permanent-magnet size [20]. For a comparison with measurements, a test setup is created to measure the damping force on a constant linear movement due to eddy current damping. For a decent verification, the remanence of the permanent magnets and the conductivity of the used aluminum plates are separately measured. Afterward, the measurements are compared to the modeling results.

II. Problem Definition

In Fig. 1(a), a rectangular plate of conductive material moving through a magnetic field induced by permanent magnets is shown [a 3-D sketch is given in Fig. 1(b)]. The permanent magnets are positioned on each side of the conductive plate. Both permanent magnets are magnetized in the positive z-direction. Furthermore, the permanent magnets are assumed to be uniformly and homogeneously magnetized, and the permanent magnets are not demagnetized in time (for instance, due to overloading or high-temperature operations). Only linear materials are used in the models, and the conductive plate is moving along the y-axis with velocity v.

A reduction in computational efforts in the semianalytical model is obtained by modeling only one magnet as is shown in Fig. 1(c). The other magnet is afterward included by means of superposition on the solution of the first magnet. In the first modeling step, it is assumed that the conducting plate is infinitely large in both the x- and y-directions, while its size

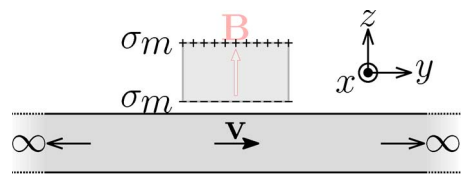

Fig. 2. Charge model for the permanent magnet as given in Fig. 1(c).

in the z-direction remains finite (see Section III-A and B). Afterward, the method of images is applied on the eddy current density derived for an infinite plate in Section III-C.

The skin effect inside the conductor is assumed to be negligible based on the low velocity of $v = 0.5\ \mathrm{m \cdot s^{-1}}$. A movement with this velocity is for the given magnet dimensions ($y_m = 26$ mm) comparable with a frequency of 20 Hz, for which the skin depth in the used aluminum is approximately 20 mm. For the observed situation, the eddy currents are originating from both the top and the bottom edge of the conducting plate. In the center of the used conducting plate ($z_p = 10$ mm), a current density is modeled that is $\leq 4\%$ smaller than the current density on the top or bottom surface. This validates the assumption of neglecting the skin effect.

III. Modeling

The modeling of the eddy current damping phenomenon consists of three steps, finding the magnetic flux density, deriving the eddy current density for an infinite conducting plate, and apply 2-D mirroring to obtain a finite conducting plate. The first two steps will be done with two different methods, namely, SPM and VPM.

A. SPM

In eddy current damping, the eddy currents are occurring based on the changing magnetic field. This magnetic field originates from two permanent magnets. In the SPM, the charge model [21], [22] is proposed to model the magnetic flux density originating from these magnets. In the charge modeling, the actual permanent magnet is replaced by magnetic equivalent charges in the volume and on the surfaces. Since only uniformly magnetized magnets are taken into account, the charge model only contains surface charges. These surface charges occur on the surfaces which are perpendicular to the magnetization direction of the permanent magnet. The obtained charge model is illustrated in Fig. 2.

Based on Green's space function, the magnetic flux density at any point in the space, due to a magnetic equivalent charge, is calculated. By integrating the magnetic equivalent charge over the full surface of the permanent magnet, the magnetic flux density due to the permanent magnet is obtained. This results in a magnetic flux density description [21] given by

$$B_x(x,y,z) = \frac{\mu_0 M_s}{4\pi} \sum_{k,n,m=0}^{1} (-1)^{k+n+m} \ln\{g+T\} \tag{1}$$

$$B_y(x,y,z) = \frac{\mu_0 M_s}{4\pi} \sum_{k,n,m=0}^{1} (-1)^{k+n+m} \ln\{-f+T\} \tag{2}$$

$$B_z(x,y,z) = \frac{\mu_0 M_s}{4\pi} \sum_{k,n,m=0}^{1} (-1)^{k+n+m} \arctan\left\{\frac{fg}{hT}\right\} \quad (3)$$

where

$$T = \sqrt{f^2+g^2+h^2} \quad (4)$$

$$f = (x - x_n) \quad (5)$$

$$g = (y - y_m) \quad (6)$$

$$h = (z - z_k) \quad (7)$$

$$M_s = \frac{B_r}{\mu_0} \quad (8)$$

x_n, y_m, and z_k represent the coordinates of the corners of the permanent magnet, and x, y, and z are the coordinates of the observation point. Furthermore, it holds that the surface charge is given by $\sigma_m = M_s = B_r/\mu_0$ since the magnet is located in free space.

The magnetic flux density of the second permanent magnet can be superimposed on the magnetic flux density from the first magnet. This is not a simple duplication of the field of the first magnet since the observation point might have a different distance to the corners of the first and the second magnet. A comparison between the modeling results for the magnetic flux density and the finite-element model is given in Section V.

For the situation as shown in Fig. 1(c) and (d), the eddy current density is modeled by solving the Maxwell–Faraday equation [23] in combination with Ohm's law. The Maxwell–Faraday equation and Ohm's law are given by

$$\nabla \times \vec{E} = -\frac{\partial \vec{B}}{\partial t} \quad (9)$$

$$\vec{J}_e = \sigma \vec{E} \quad (10)$$

where $\nabla\times$ is the curl operator, $\vec{E}$ is the electric field induced by the time-varying magnetic flux density experienced by the moving conductive plate, and σ is the electrical conductivity of the plate.

Based on the symmetry of the situation and the conductive plate thickness which is relatively small compared to the skin depth (see the last paragraph of Section II), the electric field and the eddy current density in the z-direction are negligibly small [24]. Neglecting the z-component of the eddy current density gives the x- and y-components of the eddy current density to be calculated by

$$J_x = -\sigma \int v_y \frac{\partial B_y}{\partial y} \partial z \quad (11)$$

$$J_y = \sigma \int v_y \frac{\partial B_x}{\partial y} \partial z \quad (12)$$

under the assumption that the time variation of magnetic flux density as seen by the conductive plate is only dependent on the velocity $\vec{v}$, where $\vec{v} = v_y \vec{e}_y$.

Since the eddy current density is directly computed based on the magnetic flux density originating from the permanent magnets, the fact that the eddy currents themselves introduce a magnetic flux density opposing the flux density of the permanent magnets is not taken into account.

Evaluating (11) and (12) for a magnetic flux density given by (1)–(8), the x- and y-components of the eddy current density in the conductive plate are given by

$$J_x = v_y \frac{\sigma\mu_0}{4\pi} M_s \sum_{k,n,m=0}^{1} (-1)^{k+n+m} \arctan\left(\frac{-h}{g}\right) + v_y \arctan\left(\frac{-fh}{gU}\right) \quad (13)$$

$$J_y = -v_y \frac{\sigma\mu_0}{4\pi} M_s \sum_{k,n,m=0}^{1} (-1)^{k+n+m} \ln(h+U) \quad (14)$$

with

$$U = \sqrt{f^2+g^2+h^2} \quad (15)$$

$$f = (x - x_n) \quad (16)$$

$$g = (y - y_m + v_y t) \quad (17)$$

$$h = (z - z_k) \quad (18)$$

where x, y, and z are the coordinates of the observation point while x_n, y_m, and z_k represent the coordinates of the corners of the permanent magnet.

The total eddy current density is now given by

$$\vec{J}_e = J_x \vec{e}_x + J_y \vec{e}_y + \cancel{J_z \vec{e}_z}. \quad (19)$$

The current interacts with the magnetic field which results in a damping force $\vec{F}_d$ that is counteracting the movement of the conductive material. The damping force is calculated by the Lorentz force equation

$$\vec{F}_d = \iiint_V \vec{J}_e \times \vec{B} dV. \quad (20)$$

In this paper, this integration is performed numerically. From the damping force, the damping coefficient, based on the velocity in the y-direction, is obtained by

$$\boxed{d = \frac{\vec{F}_d \cdot \vec{e}_y}{v_y}.} \quad (21)$$

B. VPM

The model based on VPM is derived in this section. The diffusion equation in terms of the magnetic vector potential is solved. This model includes the reaction field as opposed to the model from Section III-A. The magnetic vector potential $\vec{A}$ is related to the magnetic flux density as

$$\vec{B} = \nabla \times \vec{A}. \quad (22)$$

For the vector potential modeling of the simplified topology of Fig. 1(c) and (d), a current sheet model instead of the charge model is used to describe the permanent magnets. The permanent magnet is described by equivalent surface current

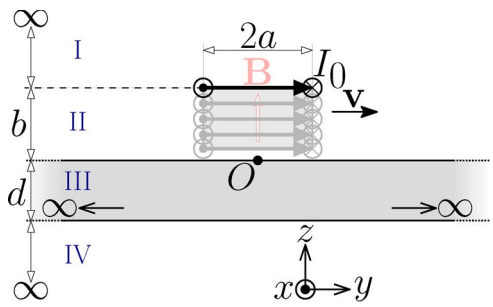

Fig. 3. Current sheet model for the permanent magnet as given in Fig. 1(c).

sheets on the sides of the permanent magnet that are parallel with the homogeneous magnetization direction [23].

The surface current density j_s used in the current sheet model is given by

$$j_s = M_s = \frac{B_r}{\mu_0} \tag{23}$$

where M_s is the magnetization of the permanent magnet and B_r is the remanent flux density of the permanent magnet.

The current sheets are discretized into a finite number of rectangular turns in the (x, y)-plane, where each rectangular turn (of size $2a \times 2c = y_m \times x_m$) carries a current I_0 which is calculated according to

$$I_0 = \frac{j_s z_m}{N} \tag{24}$$

where N is the total number of turns in which the current sheet is discretized. The solution of the total magnet is now obtained by superimposing the solution of all N rectangular turns.

The topology is simplified to Fig. 3, where four regions are considered, $i = \mathrm{I}, \ldots, \mathrm{IV}$. The current-carrying rectangular turn representing the permanent magnet is located on the boundary interface between regions I and II, and this means that the sizes of regions I and II change for each rectangular turn.

In each region, the magnetic vector potential must satisfy the diffusion equations derived from the Lorentz gauge [23] given by

$$\nabla^2 \vec{A}^{\mathrm{i}} = \mu^{\mathrm{i}} \epsilon^{\mathrm{i}} \frac{\partial^2 \vec{A}^{\mathrm{i}}}{\partial t^2} + \mu^{\mathrm{i}} \sigma^{\mathrm{i}} \frac{\partial \vec{A}^{\mathrm{i}}}{\partial t} \tag{25}$$

where $\vec{A}^{\mathrm{i}}$ is the magnetic vector potential in region i, μ is the magnetic permeability, and ϵ and σ define the electric permittivity and the electric conductivity, respectively. Equation (25) is simplified to

$$\nabla^2 \vec{A}^{\mathrm{i}} = 0, \qquad \text{for i} = \mathrm{I,\ II,\ IV} \tag{26}$$

$$\nabla^2 \vec{A}^{\mathrm{III}} = \mu^{\mathrm{III}} \sigma^{\mathrm{III}} \frac{\partial \vec{A}^{\mathrm{III}}}{\partial t} \tag{27}$$

assuming that the velocity of the conductive plate is much smaller than the speed of light. Since the magnetic vector potential only has current sources in the x- and y-directions, the current density inside the conducting plate will also be purely in the x- and y-directions. Therefore, the magnetic vector potential in the z-direction is neglected together with the J_z (equivalently with (19) and [24]). The diffusion equations of the magnetic vector potential [(26) and (27)] are rewritten to scalar differential equations given by

$$\frac{\partial^2 A_l^{\mathrm{i}}}{\partial x^2} + \frac{\partial^2 A_l^{\mathrm{i}}}{\partial y^2} + \frac{\partial^2 A_l^{\mathrm{i}}}{\partial z^2} = 0, \quad \text{for i} = \mathrm{I,\ II,\ IV} \tag{28}$$

$$\frac{\partial^2 A_l^{\mathrm{III}}}{\partial x^2} + \frac{\partial^2 A_l^{\mathrm{III}}}{\partial y^2} + \frac{\partial^2 A_l^{\mathrm{III}}}{\partial z^2} = \mu\sigma \frac{\partial A_l^{\mathrm{III}}}{\partial t} \tag{29}$$

where l represents the x- or y-component. To solve these scalar differential equations, a 3-D space–time-domain Fourier transform to x, y, and t is applied [25], [26] which is given by

$$\begin{aligned} \widetilde{A}_l^{\mathrm{i}}(k_1, k_2, z, \omega) &= \mathcal{F}_t \left\{ \mathcal{F}_y \left\{ \mathcal{F}_x \left\{ A_l^{\mathrm{i}}(x, y, z, t) \right\} \right\} \right\} \\ &= \int_{-\infty}^{\infty} \int_{-\infty}^{\infty} \int_{-\infty}^{\infty} A_l^{\mathrm{i}}(x, y, z, t) e^{-\jmath(k_1 x + k_2 y + \omega t)} \mathrm{d}x\, \mathrm{d}y\, \mathrm{d}t \end{aligned} \tag{30}$$

where $\widetilde{A}$ is the magnetic vector potential in the 3-D Fourier domain and k_1 and k_2 are the space harmonics in the x- and y-directions, respectively. By the substitution of (30) into (28) and (29), these differential equations simplify to

$$\frac{\partial^2 \widetilde{A}_l^{\mathrm{i}}}{\partial z^2} = \lambda^2 \widetilde{A}_l^{\mathrm{i}}, \quad \text{for i} = \mathrm{I,\ II,\ IV} \tag{31}$$

$$\frac{\partial^2 \widetilde{A}_l^{\mathrm{III}}}{\partial z^2} = \gamma^2 \widetilde{A}_l^{\mathrm{III}} \tag{32}$$

where

$$\lambda^2 = \left(k_1^2 + k_2^2\right) \tag{33}$$

$$\gamma^2 = \left(k_1^2 + k_2^2 - \jmath\omega\mu^{\mathrm{III}}\sigma^{\mathrm{III}}\right). \tag{34}$$

For this second-order differential equation, the solution is given by

$$\widetilde{A}_l^{\mathrm{i}} = C_l^{\mathrm{i}} \mathrm{e}^{\lambda z} + D_l^{\mathrm{i}} \mathrm{e}^{-\lambda z}, \quad \text{for i} = \mathrm{I,\ II,\ IV} \tag{35}$$

$$\widetilde{A}_l^{\mathrm{III}} = C_l^{\mathrm{III}} \mathrm{e}^{\gamma z} + D_l^{\mathrm{III}} \mathrm{e}^{-\gamma z}. \tag{36}$$

To find the solution for the constants, C_l and D_l, in (35) and (36), a set of boundary conditions is applied. Since there are two constants for the x-component and two constants for the y-component in each region, there are a total of 16 unknown constants. This means that 16 independent linear equations must be found by the boundary conditions. The first set of boundary conditions is derived from the fact that both the magnetic field and the magnetic vector potential vanish for $z \to \pm\infty$. This boundary condition results in a value for four constants, namely,

$$C_l^{\mathrm{I}} = 0, \qquad D_l^{\mathrm{IV}} = 0. \tag{37}$$

The second set of boundary conditions results from the continuity of the magnetic field on the interfaces separating the regions given by

$$\widetilde{A}_l^{\mathrm{I}}\Big|_{z=b} - \widetilde{A}_l^{\mathrm{II}}\Big|_{z=b} = \widetilde{I}_l \tag{38}$$

$$\widetilde{A}_l^{\mathrm{II}}\Big|_{z=0} - \widetilde{A}_l^{\mathrm{III}}\Big|_{z=0} = 0 \tag{39}$$

$$\widetilde{A}_l^{\mathrm{III}}\Big|_{z=-d} - \widetilde{A}_l^{\mathrm{IV}}\Big|_{z=-d} = 0 \tag{40}$$

where, on the boundary between regions I and II, the source term $\widetilde{I}_l$ is visible. This results in six independent linear equations. The third and final set of boundary conditions is derived from the possibility to choose the divergence of the magnetic vector potential [23]. Therefore, the additional condition that $\nabla \cdot \vec{A} = 0$, which is consistent with the Lorentz gauge condition [23], is used, which results in the final six linear equations. With the set of 12 independent linear equations that are derived, all constants are obtained. Solve the set of linear equations, in matrix form, given by

$$\boldsymbol{Y} = \boldsymbol{E}\boldsymbol{X} \tag{41}$$

with (42)–(44) shown at the bottom of the page, where $\widetilde{I}$ is the 3-D Fourier transform of the current description in the space–time domain, $\widetilde{I}_l$ is given in Appendix A (based on [27]), and l represents x and y, respectively. The solutions of (41)–(44) are derived with

$$\boldsymbol{X}_l = \boldsymbol{E}_l^{-1}\boldsymbol{Y}_l. \tag{45}$$

By substituting the results from (45) in (35) and (36), a general 3-D Fourier description of the magnetic vector potential in all four regions is derived. To obtain a description of the magnetic vector potential in the normal space and time domain, instead of a 2-D space harmonic and time harmonic description (in k_1, k_2, z, ω), the 3-D inverse Fourier transform is applied

$$A_l^{\mathrm{i}}(x,y,z,t) = \mathcal{F}_{k_1}^{-1}\left\{\mathcal{F}_{k_2}^{-1}\left\{\mathcal{F}_{\omega}^{-1}\left\{\widetilde{A}_l^{\mathrm{i}}(k_1,k_2,z,\omega)\right\}\right\}\right\} \tag{46}$$

where $\widetilde{A}_l^{\mathrm{i}}$ is given by (35) or (36).

The eddy current distribution $\vec{J}_e$ is derived from the magnetic vector potential according to

$$J_l = -\sigma^{\mathrm{III}}\frac{\partial A_l^{\mathrm{III}}}{\partial t}. \tag{47}$$

Since no analytical representation of the magnetic vector potential in the space–time domain is obtained, the eddy current density is solved in the 3-D Fourier domain. Therefore, (47) is transformed to the 3-D Fourier domain, which results in

$$\widetilde{J}_l = -\jmath\omega\sigma^{\mathrm{III}}\widetilde{A}_l^{\mathrm{III}}. \tag{48}$$

Its 3-D inverse Fourier transform is given by

$$J_l(x,y,z,t) = \mathcal{F}_{k_1}^{-1}\left\{\mathcal{F}_{k_2}^{-1}\left\{\mathcal{F}_{\omega}^{-1}\left\{\widetilde{J}_l(k_1,k_2,z,\omega)\right\}\right\}\right\}. \tag{49}$$

It gives a space–time description of the eddy current density. Only the inverse transformation to ω from this 3-D inverse Fourier transform is analytically obtained. The remaining two inverse Fourier transformations are calculated numerically.

From (22), the magnetic flux density is derived in the 3-D Fourier domain as

$$\widetilde{B}_x^{\mathrm{i}} = -\frac{\partial \widetilde{A}_y^{\mathrm{i}}}{\partial z} \tag{50}$$

$$\widetilde{B}_y^{\mathrm{i}} = \frac{\partial \widetilde{A}_x^{\mathrm{i}}}{\partial z} \tag{51}$$

$$\widetilde{B}_z^{\mathrm{i}} = \jmath k_1 \widetilde{A}_y^{\mathrm{i}} - \jmath k_2 \widetilde{A}_x^{\mathrm{i}}. \tag{52}$$

Equivalent to (49), the magnetic flux density components are transformed from the 3-D Fourier domain to the space–time domain. Again, only the inverse transformation to ω is obtained analytically, and the remaining two transformations are calculated numerically. With the eddy current density and the magnetic flux density in the space–time domain known, the damping force $\vec{F}_d$ is calculated according to the Lorentz law [see (20)].

C. 2-D Mirroring

From both SPM and VPM, the eddy current density for a conducting plate with infinite dimensions is obtained. The assumption used in the previous sections, an infinite conducting plate, is compensated by applying a 2-D mirroring algorithm [17], [18].

The principle of mirroring of currents is based on applying a set of boundary conditions given by

$$J_n = \sigma E_n = 0 \tag{53}$$

$$J_t = \sigma E_t \neq 0 \tag{54}$$

on the edge of the conducting material, where n and t represent the normal and the tangential direction, respectively. Aside from the primary current (i.e., the current in an infinite plate), an imaginary nonexisting current is introduced which is an exact mirror of the primary current to satisfy the boundary conditions given in (53) and (54).

For the situation of a rectangular conducting plate, many synergies to the electrostatic field distributions in a rectangular waveguide as described in [17] and [18] are found. The

$$\boldsymbol{X}_l = \left[D_l^{\mathrm{I}},\quad C_l^{\mathrm{II}},\quad D_l^{\mathrm{II}},\quad C_l^{\mathrm{III}},\quad D_l^{\mathrm{III}},\quad C_l^{\mathrm{IV}}\right]^T \tag{42}$$

$$\boldsymbol{Y}_l = \left[0,\quad 0,\quad 0,\quad \widetilde{I}_l,\quad 0,\quad 0\right]^T \tag{43}$$

$$\boldsymbol{E}_l = \begin{bmatrix} \mathrm{e}^{-\lambda b} & -\mathrm{e}^{\lambda b} & -\mathrm{e}^{-\lambda b} & 0 & 0 & 0 \\ 0 & 1 & 1 & -1 & -1 & 0 \\ 0 & 0 & 0 & \mathrm{e}^{-\gamma d} & \mathrm{e}^{\gamma d} & -\mathrm{e}^{-\lambda d} \\ \frac{\lambda}{\mu_0}\mathrm{e}^{-\lambda b} & \frac{\lambda}{\mu_0}\mathrm{e}^{\lambda b} & -\frac{\lambda}{\mu_0}\mathrm{e}^{-\lambda b} & 0 & 0 & 0 \\ 0 & \frac{\lambda}{\mu_0} & -\frac{\lambda}{\mu_0} & -\frac{\gamma}{\mu^{\mathrm{III}}} & \frac{\gamma}{\mu^{\mathrm{III}}} & 0 \\ 0 & 0 & 0 & \frac{\gamma}{\mu^{\mathrm{III}}}\mathrm{e}^{-\gamma d} & -\frac{\gamma}{\mu^{\mathrm{III}}}\mathrm{e}^{\gamma d} & -\frac{\lambda}{\mu_0}\mathrm{e}^{-\lambda d} \end{bmatrix} \tag{44}$$

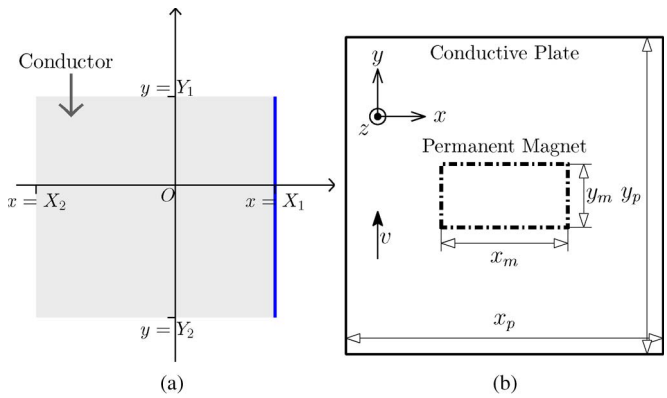

Fig. 4. Top view of the rectangular conducting plate, with the specification of (a) the edges and (b) the plate dimensions.

boundary conditions of (53) and (54) should hold for this rectangular conducting plate. However, the boundary conditions cannot be expressed by one variable, which is the situation for a cylindrical disk where mirroring is commonly applied [5], [15]. Therefore, the geometry of the conductive plate [see Fig. 4(a)] is studied in more detail.

For all four edges, $x = X_1$, $x = X_2$, $y = Y_1$, and $y = Y_2$ in Fig. 4(a), the boundary conditions should hold. Due to the assumption that the current density in the z-direction is negligible in both modeling methods, this component will not be taken into account for the mirroring process. The normal current components at each of these edges must be zero which results in a set of boundary conditions given by

$$J_x|_{x=X_1} = \sigma\, E_x|_{x=X_1} = 0 \tag{55}$$

$$J_x|_{x=X_2} = \sigma\, E_x|_{x=X_2} = 0 \tag{56}$$

$$J_y|_{y=Y_1} = \sigma\, E_y|_{y=Y_1} = 0 \tag{57}$$

$$J_y|_{y=Y_2} = \sigma\, E_y|_{y=Y_2} = 0. \tag{58}$$

For the first boundary equation (55), the x- and y-components of the electric field are mirrored at the edge highlighted in Fig. 4(a), according to

$$E_x^{(1,0)}(x,y) = -E_x^{(p)}(2X_1 - x, y) \tag{59}$$

$$E_y^{(1,0)}(x,y) = E_y^{(p)}(2X_1 - x, y) \tag{60}$$

where $E_x^{(1,0)}$ represents the imaginary electric field component with one mirror in the positive x-edge, $x = X_1$, and no mirror in the y-direction. For the edge at $x = X_2$, the same principle holds. After applying the mirrors for only the x-components, the y-components are mirrored in their corresponding edges. However, aside from the primary electric field components, the imaginary electric field components are mirrored as well. This process results in the following equations for the first mirror in the $y = Y_1$ edge

$$E_x^{(1,1)}(x,y) = -E_x^{(p)}(2X_1 - x, 2Y_1 - y) \tag{61}$$

$$E_y^{(1,1)}(x,y) = -E_y^{(p)}(2X_1 - x, 2Y_1 - y) \tag{62}$$

$$E_x^{(0,1)}(x,y) = E_x^{(p)}(x, 2Y_1 - y) \tag{63}$$

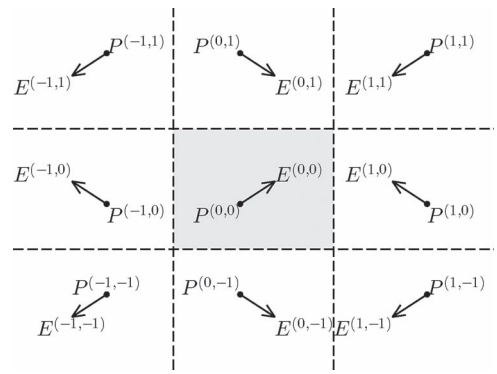

Fig. 5. Primary and imaginary electric field components after application of one layer of mirrors.

$$E_y^{(0,1)}(x,y) = -E_y^{(p)}(x, 2Y_1 - y) \tag{64}$$

$$E_x^{(-1,1)}(x,y) = -E_x^{(p)}(2X_2 - x, 2Y_1 - y) \tag{65}$$

$$E_y^{(-1,1)}(x,y) = -E_y^{(p)}(2X_2 - x, 2Y_1 - y). \tag{66}$$

After applying the mirrors in all four edges, the first layer of mirrors is obtained. This is visually illustrated in Fig. 5, in which P is a certain point in the plate and E represents the locally applicable electric field vector. The electric field vector $E^{(n_x,n_y)}$ is the primary electric field, $E^{(p)} = E^{(0,0)}$, after applying n_x mirrors in the x-direction and n_y mirrors in the y-direction, where n_x and n_y are an integer and where a positive n_x (or n_y) is a mirror in the positive x-edge (or y-edge). For each mirror applied, a small error is induced on the opposite edge of the conductor. This effect can be reduced by applying a second layer of mirrors [17], [18].

In terms of current density, a general equation for each mirrored component is given by

$$J_x^{(n_x,n_y)}(x,y) = \sigma(-1)^{n_x} E_x^{(p)}(R_x, S_y) \tag{67}$$

$$J_y^{(n_x,n_y)}(x,y) = \sigma(-1)^{n_y} E_y^{(p)}(R_x, S_y) \tag{68}$$

with

$$R_x = 2\left\lfloor \frac{|n_x|}{2} \right\rfloor \mathrm{sign}(n_x)(X_1 - X_2) + (1 - (-1)^{n_x})\, X_e + (-1)^{n_x} x \tag{69}$$

$$S_y = 2\left\lfloor \frac{|n_y|}{2} \right\rfloor \mathrm{sign}(n_y)(Y_1 - Y_2) + (1 - (-1)^{n_y})\, Y_e + (-1)^{n_y} y \tag{70}$$

where $\lfloor \cdot \rfloor$ is the floor operator

$$X_e = \begin{cases} X_1, & \text{if } n_x > 0 \\ X_2, & \text{if } n_x \le 0 \end{cases} \tag{71}$$

and

$$Y_e = \begin{cases} Y_1, & \text{if } n_y > 0 \\ Y_2, & \text{if } n_y \le 0. \end{cases} \tag{72}$$

The summation of the primary and all imaginary current sources mimics the total current density in the finite plate.

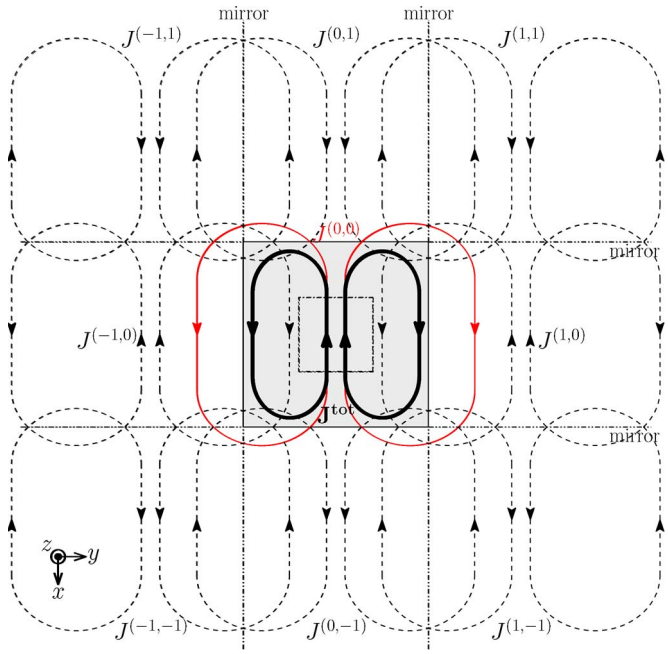

Fig. 6. Current densities involved after one layer of images is applied. (Solid) Primary (eddy) current density $J^{(0,0)}$, (dashed) the imaginary current sources, and (solid-fat line) the total current density J^{tot}.

TABLE I
BOUNDARY CONDITIONS APPLIED IN THE FINITE-ELEMENT MODEL

Name	Plane	Boundary condition
Ⓐ	$y = 75$ mm	Periodic boundary with Ⓕ
Ⓑ	$z = 75$ mm	Zero flux boundary
Ⓒ	$x = 75$ mm	Zero flux boundary
Ⓓ	$z = 0$ mm	Cyclic boundary
Ⓔ	$x = 0$ mm	Anti-cyclic boundary
Ⓕ	$y = -75$ mm	Periodic boundary with Ⓐ

For the observed situation [see Fig. 1(b)], the primary eddy current density and its images are illustrated in Fig. 6 together with the total current density J^{tot}, which is the current density for the finite conducting plate.

IV. FEM

A transient finite-element model in 3-D, using Cedrat's FLUX3D software [28], is used to verify the semianalytical models. The topology of Fig. 1(b) is simulated for a constant-velocity movement of the conductive plate along the y-axis. A reduction of computational effort is obtained by implementing periodicity along the movement axis (y-axis) in such a way that the influence between the adjacent periods can be neglected.

Furthermore, another reduction of the computational efforts is obtained by modeling only a quarter of the full topology. This is done by applying the boundaries listed in Table I. The parameters given in Table II are used in the finite-element model. An impression of the resulting finite-element model is given in Fig. 7(a).

The mesh is shown in more detail in Fig. 7(b). A second-order tetrahedron meshing is used inside the permanent magnet and in its surrounding air (8708 + 40 685 elements). For the conductive plate and the air surrounding the conductive plate, a cuboidal mesh is used (98 000 + 46 659 elements). These two meshes are connected by sliding surfaces in the air gap.

TABLE II
SPECIFICATION OF PARAMETERS USED TO MAKE A COMPARISON BETWEEN THE FINITE-ELEMENT MODEL, THE SCALAR POTENTIAL MODEL, AND THE VECTOR POTENTIAL MODEL

Variable	Value	Unit	Explanation
x_m	52	mm	Width of the PM
y_m	26	mm	Length of the PM
z_m	10	mm	Height of the PM
x_p	100	mm	Width of the conductive plate
y_p	150	mm	Length of the conductive plate
z_p	10	mm	Thickness of the conductive plate
l_{airgap}	1	mm	Airgap length
μ_0	$4\pi \cdot 10^{-7}$	H/m	Permeability of air
μ_{plate}	$4\pi \cdot 10^{-7}$	H/m	Permeability of the conductive plate
μ_{mag}	$4\pi \cdot 10^{-7}$	H/m	Permeability of the magnet
σ	$37.7 \cdot 10^6$	S/m	Conductivity of the conductive plate
B_r	1.25	T	Remanent flux density of the PMs
v_y	0.5	m/s	Velocity of the conductive plate

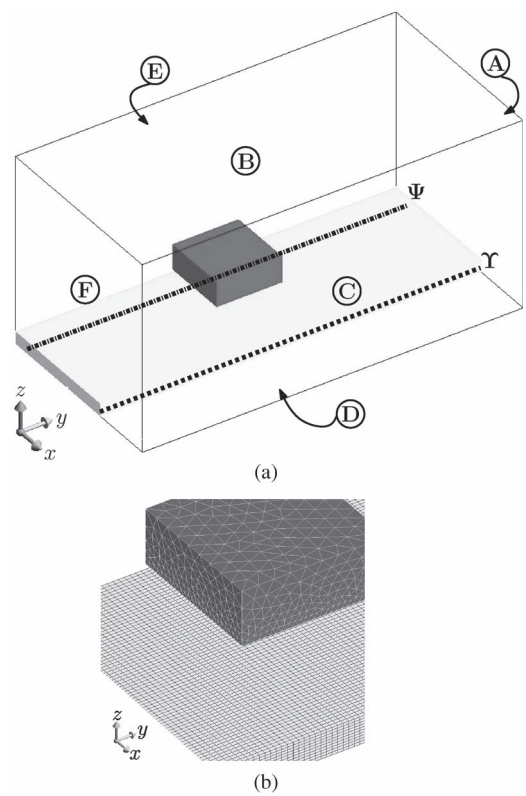

Fig. 7. (a) Finite-element model with the boundary conditions of Table I and the illustration of the paths Ψ and Υ. (b) Close-up of the mesh.

For a comparison between the finite-element model and the analytical models, two paths are created. The magnetic flux density is compared on the path Ψ which starts at (5,−75, 1) mm and stops at (5, 75, 1) mm and is illustrated in Fig. 7(a). The eddy current density is extracted on a different path Υ (which is illustrated in the same figure). The path Υ starts at (49.9,−75, 3) mm and stops at (49.9, 75, 3) mm. A numerical comparison between the finite-element model and the analytical models is obtained by evaluating the damping force in the finite-element model using the virtual work method.

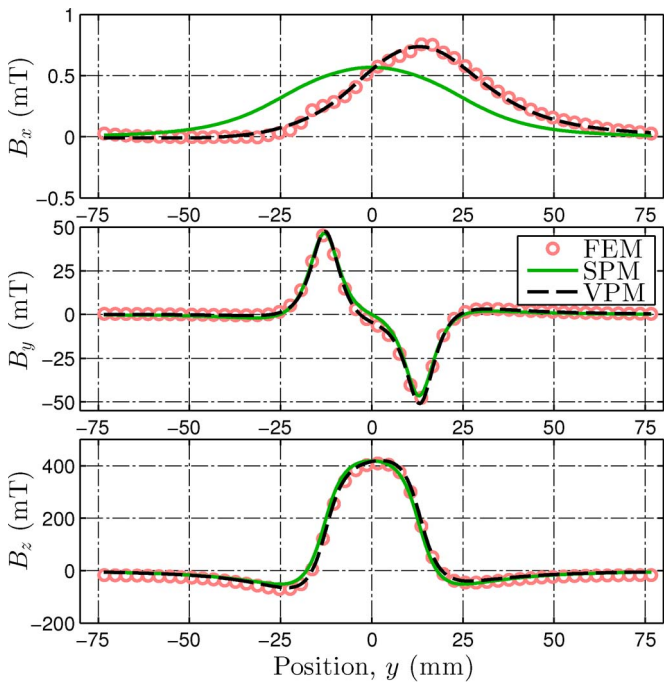

Fig. 8. Magnetic flux density $\vec{B}$ for the finite-element and semianalytical models on the path $\mathbf{\Psi}$. Given from top to bottom are the x-, y-, and z-components of the magnetic flux density, respectively. The scalar potential model is given by (SPM) and the vector potential model is given by (VPM).

V. Modeling Results

First of all, the magnetic flux densities used in the models are compared. Therefore, the magnetic flux densities for the finite-element model and the analytical models are calculated on the path $\mathbf{\Psi}$. This comparison is given in Fig. 8. It is clear (see Fig. 8) that the magnetic flux densities from the finite-element model and the SPM are not completely equal. The magnetic flux density in the x-direction differs. This is a direct effect of the counteracting magnetic field created by the eddy currents. This counteracting magnetic field also introduces the slight phase shift visible in the y- and z-directions. The magnetic flux density calculated using the VPM does include this counteracting magnetic field. This is clearly visible in Fig. 8 since the phase shift and the difference in B_x are eliminated. The magnetic flux density in the z-direction induces the eddy currents and is therefore the most important component. The z-component of magnetic flux density is correctly modeled by both the charge modeling method and the current sheet model, so both models are used to model the eddy currents for an infinite conducting plate.

For the validation of the eddy currents, the normal eddy current density component is compared on path $\mathbf{\Upsilon}$ [illustrated in Fig. 4(a) and Fig. 7(a)] on the edge of the conducting plate. The results from the transient FEM and the SPM, for an infinite plate, are given in Fig. 9, and a clearly different tendency is found between the analytical model and FEM. This occurs due to the assumption in the SPM model that the conducting plate is infinite in dimensions. After the application of one single layer of mirrors in two dimensions, the results of the SPM model (SPM-M) are in good agreement with the FEM results.

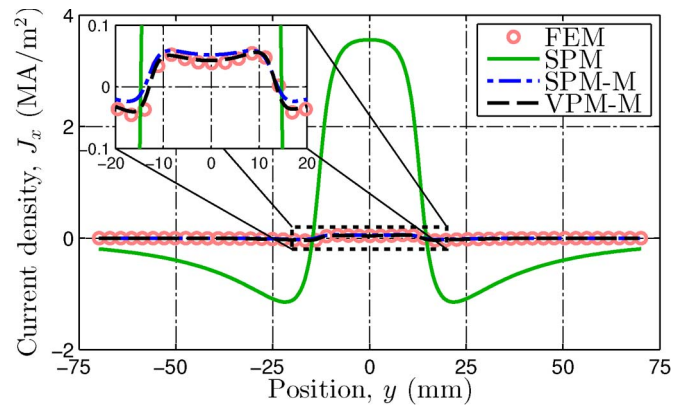

Fig. 9. Normal component of the eddy current density on the path $\mathbf{\Upsilon}$ (illustrated in Fig. 7(a) and Fig. 4) for FEM, the scalar potential model (SPM), the scalar potential model with one layer of mirrors (SPM-M), and the vector potential model with one layer of mirrors (VPM-M). The dimensions are: $x_p = 50$, $y_p = 140$, $x_m = 52$, $y_m = 26$, $z_p = z_m = 10$ mm, and $\sigma = 37.7$ MS/m and are illustrated in Fig. 4(b).

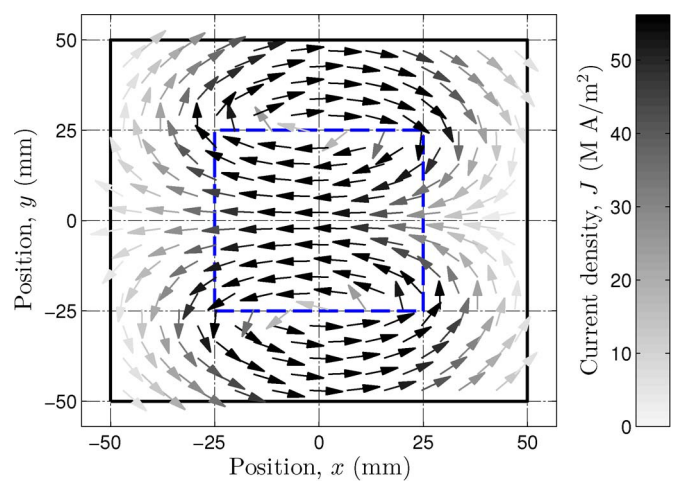

Fig. 10. Eddy current density in the xy-plane at $z = 4$ mm (1 mm below the surface of the plate) for the scalar potential model with one layer of mirrors (SPM-M). The properties used are as follows: $x_p = y_p = 100$, $x_m = y_m = 50$, $z_p = z_m = 10$ mm, $v_y = 0.5$ m/s, $B_r = 1.5$ T, and $\sigma = 37.7$ MS/m.

A slightly better agreement is found for the VPM with one layer of mirrors applied (VPM-M).

A visualization of the eddy current density in the xy-plane 1 mm under the surface of the conducting plate calculated using the scalar potential model, including one layer of mirrors, is given in Fig. 10 for the conductive plate moving in the y-direction with $v_y = 0.5$ m/s. The solid and dashed squares represent the plate and magnet, respectively.

Even though the VPM-M model gives a slightly better agreement with FEM than the SPM-M, the SPM-M is chosen for the further force calculations because of the calculation time. With the current implementation, the calculation time is reduced from > 5 h (for 3-D FEM) to $\approx .5$ h for the VPM-M model, while SPM-M is finished in ≈ 12 s. Without taking the mirrors into account, the calculation times are reduced to ≈ 2 min and ≈ 1.5 s for VPM and SPM, respectively.

The damping coefficient has been calculated as a function of the dimensions of the conductive plate [see Fig. 4(b)] with respect to the permanent-magnet dimensions. The results of a variation in the dimensions of the conducting plate are given in

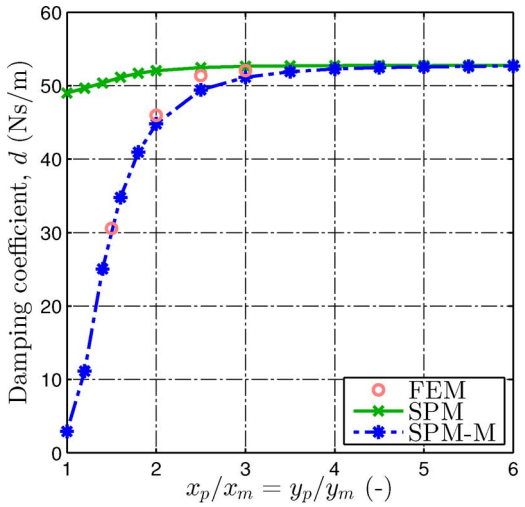

Fig. 11. Damping coefficient for a variation of the plate dimensions with respect to the magnet dimensions. The dimensions are illustrated in Fig. 4(b), and $x_m = 50$ mm.

Fig. 11, where SPM is the analytical model assuming an infinite plate, SPM-M is the analytical model for a finite plate (one layer of images is applied), and FEM represents the results obtained by the FEM.

When assuming an infinite conductor, an error smaller than 15% is made compared to FEM if the conducting plate has at least twice the dimensions of the permanent magnets. For conducting plates with relatively small dimensions, the accuracy of the damping coefficient is increased by applying multiple layers of images. The error that remains at twice the permanent-magnet dimensions is less than 3%.

For the modeling with the SPM, it is assumed that the counteracting magnetic field which is caused by the eddy currents inside the conducting plate is negligible. Using FEM, it is confirmed that this assumption results in an error of less than 10% for a velocity up to 2 m/s for the given situation (see Appendix B). For the velocity used in this paper, 0.5 m/s, and the geometry as given in Fig. 1(b), the approximated skin depth is 20 mm. This implies that the skin effect in the used conducting plate, having a thickness of 10 mm, is negligible (see the last paragraph of Section II). This is consistent with the assumptions made for both semianalytical models and is consistent with the findings from the finite-element model.

VI. Measurements

A test setup is created to measure the eddy current damping force due to a linear movement of a conducting sheet between the permanent magnets (see Fig. 12). A load cell, an ATI mini40R-2 [29], is mounted on the moving part of a linear air bearing. The linear mover is actuated by an iron-cored linear permanent-magnet motor with concentrated windings and is controlled to a constant velocity based on the displacement measurements of a linear encoder with a resolution of 1 μm. On the stator part of the assembly, the magnets are mounted with the possibility to change the air-gap length between the conducting plate and the permanent magnets. On top of the force cell, the conducting plate is mounted, and therefore, the damping force acting on the conducting plate is directly

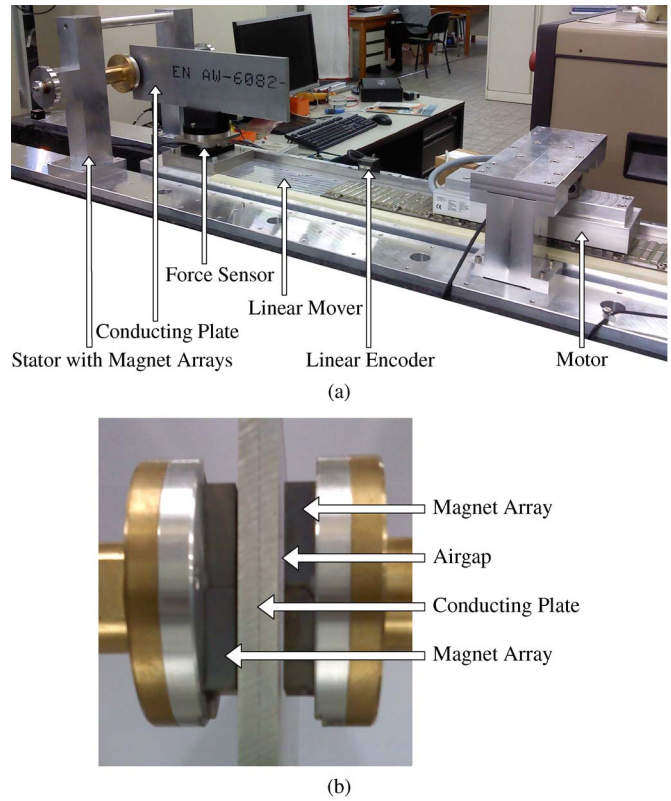

Fig. 12. Test setup used for measuring the eddy current damping due to a linear constant-velocity movement of a conducting plate through the permanent magnets. (a) Global test setup overview. (b) Close-up of the eddy current damper parts.

measured by the sensor. The full test setup is shown in Fig. 12, and a close-up of the eddy current damper itself is given in Fig. 12(b).

For each configuration, i.e., a conducting plate with one air gap, five measurements are taken, from which the mean value is used after eliminating the highest and lowest values. To ensure that the semianalytical model is describing a situation which is as close to the real measurement situation as possible, the parameters used in the semianalytical model are extracted from the test setup. All dimensions of the permanent magnets and the conducting plate are measured as well as the length of the air gap, the remanent flux density of the permanent magnet, B_r, and the conductivity of the plate, σ.

In the semianalytical models, the permanent magnet is modeled using an equivalent charge or current sheet model placed in the air. Therefore, it is not possible to directly take the permeability of the permanent magnet into account in the modeling. However, according to Rovers *et al.* [30], the relative permeability of a permanent magnet can be compensated by reducing the remanent flux density of the magnet as given by

$$B_{\text{model}} = \frac{2B_{\text{real}}}{\mu_{r,\text{mag}} + 1} \tag{73}$$

where B_{real} is the remanent flux density of the permanent magnet while B_{model} is the remanent flux density used in the model.

The conductivity of the aluminum plate used, AL-6082, is specified for a very broad range. This range can cause up

TABLE III
MODELING PARAMETERS USED FOR COMPARISON WITH MEASUREMENTS

Variable	Value	Unit	Explanation
x_m	$51.9 \pm .05$	mm	Width of the PM
y_m	$25.95 \pm .05$	mm	Length of the PM
z_m	$9.95 \pm .05$	mm	Height of the PM
x_p	$50/100/150 \pm .1$	mm	Width of the conductive plate
y_p	$350 \pm .1$	mm	Length of the conductive plate
z_p	$10 \pm .1$	mm	Thickness of the conductive plate
l_{airgap}	$1.0 \pm .1$	mm	Airgap length
μ_0	$4\pi \cdot 10^{-7}$	H/m	Permeability of air
μ_{plate}	μ_0	H/m	Permeability of the conductive plate
μ_{mag}	$1.03\mu_0 \pm 0.01\mu_0$	H/m	Permeability of the magnet
σ	$25.5 \pm .5$	MS/m	Conductivity of the conductive plate
B_{meas}	$1.25 \pm .01$	T	Measured Remanent flux density
v_y	$0.1/0.2/0.3$	m/s	Velocity of the conductive plate

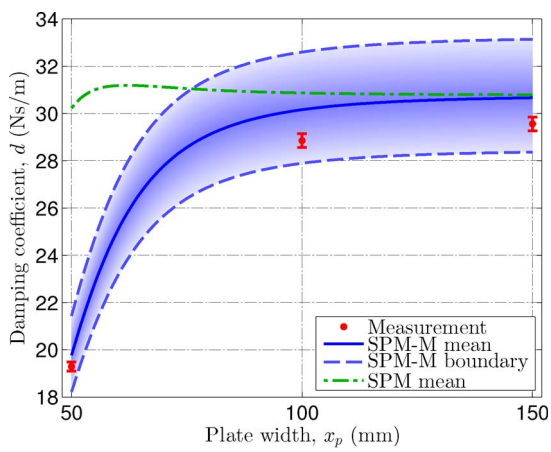

Fig. 13. Damping coefficient d for a variation of plate width, x_p, for the SPM-based analytical model (SPM), the SPM-based analytical model with one layer of mirrors (SPM-M), and the measurements (including a 1% confidence interval based on the manufacturer specifications).

to $\pm 15\%$ difference when using the mean of the specified range. To reduce this difference, the conductivity of the actual aluminum plates is measured and specified to the range of $25 \leq \sigma \leq 26$ MS/m.

For each parameter of the model, a mean value is determined together with an uncertainty bound. The uncertainty bound is chosen based on the inaccuracy during the determination of the parameters and the variations in the production processes as specified by the manufacturer.

The chosen parameters, together with their uncertainty bounds, are listed in Table III.

In Fig. 13, the damping coefficient is extracted from the measurements with a constant velocity of $v_y = 0.2$ m/s for a variation in the plate width. In the same figure, the results of the semianalytical model with the mean value of the parameters as specified in Table III are given. Around the mean modeling results, an uncertainty boundary is given which is limited by the uncertainty on the parameters as specified in the table. The measurements are given in the figure as well, including a confidence interval of 1% based on the manufacturer specifications. The measurements are well within the boundary limits of the analytical model with one layer of mirrors (SPM-M). The measurement discrepancy with respect to the mean value of the SPM-M model is below 5%. Therefore, it is assumed that the presented model is in agreement with the measurements.

TABLE IV
MEASURED DAMPING COEFFICIENT FOR DIFFERENT VELOCITIES AND A VARIATION IN PLATE WIDTH

	$v_y = 0.1$ m/s	$v_y = 0.2$ m/s	$v_y = 0.3$ m/s
$x_p = 50$ mm	19.2 Ns/m	19.3 Ns/m	19.3 Ns/m
$x_p = 100$ mm	28.7 Ns/m	28.9 Ns/m	28.8 Ns/m
$x_p = 150$ mm	29.5 Ns/m	29.6 Ns/m	29.6 Ns/m

Another aspect which can be gained from analyzing the results in Fig. 13 is the large difference between the measurement and the analytical model without the mirrors (SPM). Particularly for the lower values of the plate width, the analytical model without mirrors is incapable of predicting a realistic damping coefficient.

Furthermore, in the modeling process, it is assumed that the damping coefficient is independent of the velocity (see Appendix B). This assumption is verified with measurements as well. The maximum velocity used in the measurements is limited by the setup. The measurement results are given in Table IV. For a fixed plate width, the measurements on the three velocities are in a very good agreement with each other, which indicates the independence of the damping coefficient for velocity variations in the considered velocity range. Therefore, the results in this table prove the validity of the assumption.

VII. CONCLUSION

The magnetic flux density inside a conducting plate that is moving between cuboidal magnets is derived with two different modeling methods, SPM and VPM. Both modeling methods obtain a good agreement for the z-component of the magnetic flux density. For the B_x, the vector potential model is clearly more accurate since it includes the counteracting magnetic field created by the induced eddy currents. Aside from the magnetic flux density, the eddy current density on an infinite conducting plate is calculated with both modeling methods. For both analytical models, the eddy current density is in a good agreement. Afterward, the method of images in two dimensions is applied to the eddy current density of an infinite conducting plate to obtain the eddy current density on a finite conducting plate. Applying the method of images in two dimensions significantly reduces the difference in the damping coefficient obtained from the analytical model and the finite-element analysis (from 56.4% to 4.0%). Therefore, it is concluded that the method of images in two dimensions reduces the modeling error in eddy current dampers with permanent magnets and a conductive plate with finite dimensions. Furthermore, it is shown that, for a conducting plate with at least twice the dimensions of the permanent magnets, only a small error, $< 15\%$, is made if an infinite plate is assumed. For a conducting plate smaller than twice the permanent-magnet dimensions, a model with the application of the method of images must be used, and this will reduce the error to less than 3%. Based on the performed measurements, it is concluded that the shown analytical model with the method of images applied is capable of accurately predicting the damping coefficient d. The mean value of the

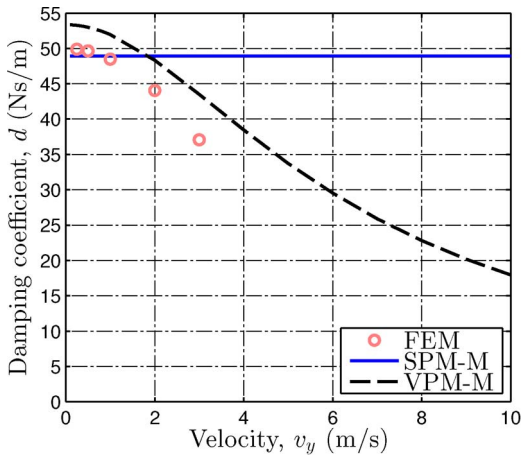

Fig. 14. Damping coefficient for a variation of the velocity of the conducting plate by the SPM-based analytical model with one layer of mirrors (SPM-M), the vector potential model with mirrors (VPM-M), and by the finite-element model. The parameters used are: $x_p = 100$ mm, $y_p = 100$ mm, $x_m = 50$ mm, $y_m = 20$ mm, $z_p = z_m = 10$ mm, and $\sigma = 37.7$ MS/m and are illustrated in Fig. 4(b).

analytical model has less than 5% discrepancy with respect to the measurements.

Appendix A
3-D Fourier Transform of the Current

The 3-D Fourier transform of the current is given by

$$\widetilde{I}_x = \mathcal{F}_t\left\{\mathcal{F}_x\left\{\mathcal{F}_y\{I_x\}\right\}\right\} = \frac{8\jmath\pi I_0}{k_1}\sin(k_1 c)\sin(k_2 a)\delta(\omega + k_2 v_y) \tag{74}$$

$$\widetilde{I}_y = \mathcal{F}_t\left\{\mathcal{F}_y\left\{\mathcal{F}_x\{I_y\}\right\}\right\} = \frac{-8\jmath\pi I_0}{k_2}\sin(k_1 c)\sin(k_2 a)\delta(\omega + k_2 v_y) \tag{75}$$

where $a = y_m/2$ and $c = x_m/2$ represent the magnet dimensions (see Fig. 3), I_0 is the current per turn as calculated by (24), and k_1 and k_2 are the space harmonic frequencies in the x- and y-directions, respectively. Furthermore, the ω is the time frequency, $\jmath$ is the imaginary unit, and δ represents the Dirac delta function.

Appendix B
Velocity Variation

In the modeling, the velocity of the conducting sheet is assumed to be low enough to neglect the counteracting magnetic field. To validate this assumption, in Fig. 14, the velocity is varied for constant geometric parameters (magnet and plate dimensions) and conductivity ($x_p = 100$ mm, $y_p = 100$ mm, $x_m = 50$ mm, $y_m = 20$ mm, $z_p = z_m = 10$ mm, and $\sigma = 37.7$ MS/m), and the parameters are illustrated in Fig. 4(b). The results of the SPM model with mirrors (SPM-M), the vector potential model with mirrors (VPM-M), and the finite-element model are given.

The SPM-M model, used in the comparison between the analytical model and the measurements, is within $\pm 10\%$ error with respect to the finite-element model for a velocity ≤ 2 m/s.

Furthermore, the figure shows that the VPM-M model has a very good description of the tendency found in the FEM model; however, a constant offset of $\approx 5\text{N}\cdot\text{s/m}$ is visible. Regardless of the offset, the VPM-M model will be better suited at high velocities than the SPM-M model.

References

[1] P. Handgruber, A. Stermecki, O. Biro, A. Belahcen, and E. Dlala, "3-D eddy current analysis in steel laminations of electrical machines as a contribution for improved iron loss modeling," in *Proc. 20th ICEM*, Sep. 2012, pp. 16–22.

[2] P. Madina, J. Poza, G. Ugalde, and G. Almandoz, "Analysis of non-uniform circumferential segmentation of magnets to reduce eddy-current losses in SPMSM machines," in *Proc. 20th ICEM*, Sep. 2012, pp. 79–84.

[3] M. Nabavi and S. Nihtianov, "Eddy-current sensor interface for advanced industrial applications," *IEEE Trans. Ind. Electron.*, vol. 58, no. 9, pp. 4414–4423, Sep. 2011.

[4] X. Cui and J. Haldemann, "Analytical time-harmonic approach to calculate rotor eddy-current losses due to stator harmonics," in *Proc. 20th ICEM*, Sep. 2012, pp. 85–91.

[5] H. Sodano, J. Bae, D. Inman, and W. Belvin, "Improved concept and model of eddy current damper," *Trans. ASME*, vol. 128, no. 3, pp. 294–302, Jun. 2006.

[6] M. Barcaro, N. Bianchi, and F. Magnussen, "Permanent-magnet optimization in permanent-magnet-assisted synchronous reluctance motor for a wide constant-power speed range," *IEEE Trans. Ind. Electron.*, vol. 59, no. 6, pp. 2495–2502, Jun. 2012.

[7] N. Hodgins, O. Keysan, A. McDonald, and M. Mueller, "Design and testing of a linear generator for wave-energy applications," *IEEE Trans. Ind. Electron.*, vol. 59, no. 5, pp. 2094–2103, May 2012.

[8] J. Potgieter and M. Kamper, "Torque and voltage quality in design optimization of low-cost non-overlap single layer winding permanent magnet wind generator," *IEEE Trans. Ind. Electron.*, vol. 59, no. 5, pp. 2147–2156, May 2012.

[9] J. Rovers, J. Jansen, J. Compter, and E. Lomonova, "Analysis method of the dynamic force and torque distribution in the magnet array of a commutated magnetically levitated planar actuator," *IEEE Trans. Ind. Electron.*, vol. 59, no. 5, pp. 2157–2166, May 2012.

[10] N. Niguchi and K. Hirata, "Cogging torque analysis of magnetic gear," *IEEE Trans. Ind. Electron.*, vol. 59, no. 5, pp. 2189–2197, May 2012.

[11] J. H. J. Potgieter and M. Kamper, "Evaluation of calculation methods and the effect of end-winding inductance on the performance of non overlap winding PM machines," in *Proc. 20th ICEM*, 2012, pp. 243–249.

[12] R. Vermaak and M. Kamper, "Design aspects of a novel topology air-cored permanent magnet linear generator for direct drive wave energy converters," *IEEE Trans. Ind. Electron.*, vol. 59, no. 5, pp. 2104–2115, May 2012.

[13] J. Aubry, H. Ben Ahmed, and B. Multon, "Sizing optimization methodology of a surface permanent magnet machine-converter system over a torque-speed operating profile: Application to a wave energy converter," *IEEE Trans. Ind. Electron.*, vol. 59, no. 5, pp. 2116–2125, May 2012.

[14] J. W. Jansen, E. A. Lomonova, and J. M. M. Rovers, "Effects of eddy currents due to a vacuum chamber wall in the airgap of a moving-magnet linear actuator," *J. Appl. Phys.*, vol. 105, no. 7, pp. 07F111-1–07F111-3, Apr. 2009.

[15] J. Janssen, B. Gysen, J. Paulides, and E. Lomonova, "Advanced electromagnetic modeling applied to anti-vibration systems for high precision and automotive applications," *Int. Compumag Soc. Newsl.*, vol. 1, no. 19, pp. 3–16, Jan. 2012.

[16] K. Lee, C. Kim, and K. Park, "Development of an eddy-current-type magnetic floor hinge," *IEEE Trans. Ind. Electron.*, vol. 53, no. 2, pp. 561–568, Apr. 2006.

[17] J. Kunz and P. L. Bayley, "Some applications of the method of images—I.," *Phys. Rev.*, vol. 17, no. 2, pp. 147–156, Feb. 1921.

[18] C. M. Hebbert, "Some applications of the method of images—II.," *Phys. Rev.*, vol. 17, no. 2, pp. 157–160, Feb. 1921.

[19] S. Jang, S. Lee, and S. Jeong, "Characteristic analysis of eddy-current brake system using the linear Halbach array," *IEEE Trans. Magn.*, vol. 38, no. 5, pp. 2994–2996, Sep. 2002.

[20] K. J. W. Pluk, B. L. J. Gysen, J. L. G. Janssen, E. A. Lomonova, and J. W. Jansen, "Modeling of a finite, rectangular, conducting plate in an eddy current damper," in *Proc. 20th ICEM*, Sep. 2012, pp. 2846–2851.
[21] G. Akoun and J. P. Yonnet, "3-D analytical calculation of the forces exerted between two cuboidal magnets," *IEEE Trans. Magn.*, vol. MAG-20, no. 5, pp. 1962–1964, Sep. 1984.
[22] J. W. Jansen, J. L. G. Janssen, J. M. M. Rovers, J. J. H. Paulides, and E. A. Lomonova, "(Semi-) analytical models for the design of high-precision permanent magnet actuators," *Int. Compumag Soc. Newsl.*, vol. 16, no. 2, pp. 4–17, 2009.
[23] E. P. Furlani, *Permanent Magnet and Electromechanical Devices*. Amsterdam, The Netherlands: Elsevier, 2001.
[24] J.-Y. Chen, J.-B. Zhou, G. Meng, and W.-M. Zhang, "Evaluation of eddy-current effects on diamagnetic bearings for microsystems," *IEEE Trans. Ind. Electron.*, vol. 56, no. 4, pp. 964–972, Apr. 2009.
[25] J. Krotsch and B. Piepenbreier, "Radial forces in external rotor permanent magnet synchronous motors with non-overlapping windings," *IEEE Trans. Ind. Electron.*, vol. 59, no. 5, pp. 2267–2276, May 2012.
[26] F. Neves, H. de Souza, F. Bradaschia, M. Cavalcanti, M. Rizo, and F. Rodriguez, "A space-vector discrete Fourier transform for unbalanced and distorted three-phase signals," *IEEE Trans. Ind. Electron.*, vol. 57, no. 8, pp. 2858–2867, Aug. 2010.
[27] S. Panas and E. E. Kriezis, "Eddy current distribution due to a rectangular current frame moving above a conducting slab," *Arch. Elektrotech.*, vol. 69, no. 3, pp. 185–191, 1986.
[28] *FLUX 11.1.2, User's Guide*, Cedrat, Meylan, France, 2013.
[29] *ATI mini40R-2, 6-dof force cell*, ATI Industrial Automation, Apex, NC, USA, 1989.
[30] J. M. M. Rovers, J. W. Jansen, and E. A. Lomonova, "Modeling of relative permeability of permanent magnet material using magnetic surface charges," *IEEE Trans. Magn.*, vol. 49, no. 6, pp. 2913–2919, Jun. 2013.

K. J. W. (Kevin) Pluk (S'12) was born in Prinsenbeek, The Netherlands, in 1986. He received the M.Sc. degree in electrical engineering from the Eindhoven University of Technology (TU/e), Eindhoven, The Netherlands, in 2011, where he is currently working toward the Ph.D. degree in the Electromechanics and Power Electronics Group, Department of Electrical Engineering.

His focus is on the electromagnetic crosstalk between actuators and magnetic shielding.

T. A. (Tom) van Beek was born in Arnhem, The Netherlands, in 1989. He received the B.Eng. degree in electrical engineering from the Hogeschool van Arnhem en Nijmegen, Nijmegen, The Netherlands, in 2010. He is currently working toward the M.Sc. degree in the Electromechanics and Power Electronics Group of the Department of Electrical Engineering, Eindhoven University of Technology (TU/e), Eindhoven, The Netherlands.

His focus is on eddy current damping.

J. W. (Helm) Jansen (M'07) received the M.Sc. degree (*cum laude*) in electrical engineering in 2003 and the Ph.D. degree in magnetically levitated planar actuator technology from the Eindhoven University of Technology, Eindhoven, The Netherlands.

He then joined the Electromechanics and Power Electronics Group, Eindhoven University of Technology, where he is currently an Assistant Professor. His research interests include magnetic levitation and the analysis and design of linear and planar actuators.

E. A. (Elena) Lomonova (SM'07) was born in Moscow, Russia. She received the M.Sc. (*cum laude*) and Ph.D. (*cum laude*) degrees in electromechanical engineering from the Moscow State Aviation Institute (TU), Moscow, in 1982 and 1993, respectively.

She is currently a Full Professor with the Eindhoven University of Technology, Eindhoven, The Netherlands. She has worked on electromechanical actuator design and optimization and development of advanced mechatronics systems.